Auxiliary text, figures, and tables

"High-resolution reconstructions of Pacific-North America plate motion: 20 Ma to present"

by C. DeMets & S. Merkouriev

Overview

The supplementary material includes information, figures, and files that are referred to within or are relevant to the main document. These include a brief description of our processing method for the raw GPS data, maps of the horizontal and vertical components of the North America plate GPS velocities used for part of the analysis, a table of rotations for the Sierra Nevada microplate relative to the Pacific plate, figures relevant to our Bayesian analysis of Pacific-Antarctic rotations and our comparative analysis of spline smoothing and Bayesian noise reduction on the rotations used for the analysis, and two text files with North America and GPS site velocities that were used for the analysis.

List of text file contents

1. *North_America_GPS.txt*: This file tabulates the horizontal and vertical velocity components of the 908 GPS stations that were used to estimate the best-fitting North America plate angular velocity relative to IGS08 given in Table 1 of the main document. More information is provided in the file header and footnotes.

2. *Pacific_GPS.txt*: This file tabulates the horizontal velocity components of the 27 GPS stations that were used to estimate the best-fitting Pacific plate angular velocity relative to IGS08 given in Table 1 of the main document. More information is provided in the file header and footnotes.

I. GPS data processing methods

All raw GPS observations used in this study were processed with GIPSY software version 6.3 from the Jet Propulsion Laboratory (JPL) using a precise-point-positioning analysis strategy (Zumberge *et al*. 1997). Our analysis incorporates *a priori* constraints on the tropospheric hydrostatic and wet delays from Vienna Mapping Function (VMF1) parameters (http://ggosatm.hg.tuwien.ac.at), elevation- and azimuthally-dependent GPS and satellite antenna phase center corrections from IGS08 ANTEX files (available via ftp from sideshow.jpl.nasa.gov), FES2004 corrections for ocean tidal loading (http://holt.oso.chalmers.se), and second-order ionospheric corrections. Phase ambiguities were resolved using GIPSY's single-station ambiguity resolution feature (Bertiger *et al*. 2010).

Daily no-net-rotation station location estimates were transformed to IGS08 with seven-parameter Helmert transformations from JPL. Spatially correlated noise between GPS sites on the North America Plate was then estimated from the coordinate time-series of well-behaved continuous stations in the plate interior and removed from the time series of all of the sites (Marquez-Azua & DeMets 2003). The day-to-day variations in both the northing and easting components of the station coordinates average 1.1 mm (1-sigma) and range from 0.65 mm to 2.5 mm.

Station velocities were estimated via linear regressions of the daily horizontal and vertical components of the GPS station locations and incorporate any necessary offsets from known or unknown sources.

II. North America plate GPS velocity field and solution robustness

Figures A1 and A2 show the horizontal velocities (Fig. A1a) and vertical rates (Fig. A1b and Fig. A2) for all North American GPS stations for which which we process daily GPS data (see the previous section). Each horizontal site velocity in Fig. A1a has been transformed to a frame of reference fixed to the North America plate by subtracting from each velocity the motion of the North America plate in IGS08 at the site, as estimated with the best-fitting angular velocity from Table 1 of the main document. Hereafter, we refer to these as residual velocities. The red arrows identify the 908 stations whose velocities were used to determine the best-fitting North America-IGS08 angular velocity. The blue arrows identify the GPS sites that are located in deforming areas of the North America plate.

Section 2.2 of the main document briefly describes the areas of North America from which we used site velocities to estimate the plate angular velocity, namely, the areas of the plate where no deformation occurs. Other authors have defined the present western and southern limits of undeformed North America plate lithosphere based on deformation patterns that are associated with the major tectonic features in these regions (*e.g.* Bennett *et al.* 1999; Marquez-Azua & DeMets 2009; Kreemer *et al.* 2010). Those limits are described briefly in Section 2.2 of the main document.

Identifying areas of the plate interior that are unaffected by glacial isostatic adjustment (GIA) is more challenging because of the lack of precise *a priori* information about the full extent of the area that is presently affected by GIA. In southern Canada and the northern United States, GPS sites that move consistently southward to southwestward in a frame of reference that is tied to the plate interior are diagnostic of areas of the plate with measurable horizontal GIA effects (*e.g.* Calais *et al.* 2006; Sella *et al.* 2007). The pattern of residual velocities can thus be used to approximate the areas of the plate interior where GIA is minimal or absent. Unfortunately, the residual station velocities cannot be determined accurately without first knowing which areas of the plate are unaffected by GIA, thereby introducing a circularity into efforts to use residual GPS velocities to define the limits of the areas that are affected by GIA and hence define the subset of the site velocities that can be used to derive an estimate of the North America-IGS08 angular velocity that is unbiased by GIA.

To cope with this circularity, we explored how the pattern of residual GPS site velocities changes as a function of the three different models for the assumed location of the transition between undeforming areas of the plate interior and areas impacted by isostatic rebound. If we simplistically assume that the transition is well approximated by the U.S.-Canada border and thus use velocities of the 1461 GPS sites from our velocity solution that are located south of the border and east of the Rocky Mountains to estimate the North America plate angular velocity relative to IGS08, then southward to southwestward residual site velocities are observed at locations as far south as northern Iowa, southern Wisconsin, central/northern Ohio, and southern Pennsylvania. If we instead assume that the transition is located $\approx$300 km south of the border and thus use a more geographically-limited subset of 908 GPS sites to estimate the North America plate angular velocity, there is almost no change in the resulting pattern of residual velocities. The residual velocity pattern is thus relatively robust with respect to the geographic subset of the GPS stations that are used to estimate the North America-IGS08 angular velocity and is thus a useful, though imperfect,

basis for defining the geographic subset of the GPS stations that can be used to estimate the North America-IGS08 angular velocity.

The vertical GPS site rates that are illustrated in Fig. A1B and Fig. A2 provide a useful independent means for identifying parts of the continent that are impacted by glacial isostatic rebound. Broad areas of slowly subsiding crust that are defined by the vertical rates within three, non-overlapping transects that extend SSW from Hudson Bay (Fig. A2) clearly reveal the geographic extent of the collapsing glacial forebulge. The hinge line that separates the subsiding forebulge from areas where isostatic rebound occurs is approximately defined by the 0-km distance line in the map in Fig. A2. The subsiding forebulge extends southwards to central Missouri, Kentucky, and North Carolina in the central United States, well beyond the areas where the southward to southwestward horizontal station motions diagnostic of GIA are recognized (Fig. A1A).

As a test, we assumed that measurable horizontal effects of GIA extend one degree farther south in the central and eastern United States than is suggested by the residual velocities for the two models described above. We inverted the velocities of the 773 GPS sites that are located on the nominally undeforming part of the plate interior to find their best-fitting North America-IGS08 angular velocity. Both the resulting angular velocity and its associated pattern of residual site velocities differ insignificantly from those for the previously described solution in which the geographic cutoff between the deforming and undeforming areas is assumed to be one degree of latitude north of that assumed in this model. The angular velocities for this and the previous solution suggest linear velocities in western California that differ by less than 0.01 mm yr^{-1} in rate and by 0.01 $^\circ$ in direction. This miniscule difference is too small to impact any of the conclusions reached in our kinematic analysis and moreover indicates that our estimate of the North America-IGS08 angular velocity is highly robust to modest changes in the geographic limits that we use to identify areas of North America with insignificant horizontal GIA effects.

Based on the results described above, we use the 908 GPS velocities from the area indicated in Fig. A1 (defined by the red arrows) to determine the preferred North America-IGS08 angular velocity (Table 1 in the main document). Only nine stations from Canada, all in the province of Nova Scotia, exhibit no evidence for GIA. All nine are included in our solution.

III. Changes in circuit plate motions from REDBACK analyses

Fig. A3 summarizes the likelihoods that changes occurred in the locations of poles (dashed lines) and angular opening rates (solid lines) at different times during the past 20 Myr for all three plate pairs in the global plate circuit. These indicate when significant changes occurred in the interval velocities shown in Fig. 7 of the main document. The likelihood estimates for all three plate pairs were determined from REDBACK analyses of the original best-fitting rotations for the three plate pairs that were variously done by DeMets *et al*. (2015*ab*) and herein.

IV. Pacific-North America spline-smoothed versus other solutions

Figures A4 and A5 compare the best-fitting Pacific-North America rotation estimates and their associated interval velocities to Bayesian noise-reduced and spline-smoothed rotations and interval velocities. Readers are referred to Section 6.3 of the main document for a discussion of most of the main results illustrated in these figures. The spline-smoothed poles, which were derived using the cross-validation smoothing method discussed in the main document, reproduce the north-to-south movement of the best-fitting and noise-reduced rotation poles during the past 20 Myr (Fig. A4).

Four sets of interval velocities are depicted in Fig. A5, two of which are derived from the best-

fitting finite rotations in Table 4 of the main document and the other two of which are determined from the Bayesian noise-reduced stage angular velocities in Table 5 of the main document and the spline-smoothed rotations (not given). Below, we briefly discuss these interval velocities in more detail than was possible in the main document.

The noisiest interval velocities shown in Fig. A5 (red triangles) were derived by differentiating progressively older pairs of best-fitting finite rotations from Table 4 and using the resulting time sequence of interval angular velocities to estimate linear velocities at a fiducial point on the San Andreas Fault. By design, these best-fitting stage angular velocities span the shortest intervals that are sampled by our rotation sequence and thus have the lowest ratio between the interval opening angles and their uncertainties (the signal to noise). In addition, the errors in the interval angular velocities are anti-correlated at their shared time boundaries, which adds additional noise. For example, assuming that the pole of opening is stationary for hypothetical times t_1, t_2, and t_3 in a rotation sequence, if opening angle Ω_{t2} for the intermediate-age finite rotation for t_2 is overestimated by a small angle $\delta\theta_2$, then the error $\delta\theta_2$ will propagate in equal, but opposite fashion in the interval angles $\Delta\Omega_{t1-t2}$ and $\Delta\Omega_{t2-t3}$ that describe motion from times t_1 to t_2 and t_2 to t_3. The two interval angles will thus be respectively overestimated and underestimated by the angle $\delta\theta_2$. Conversion of the interval angles to interval angular rotation rates also adds noise given that any errors in the ages estimated for the magnetic reversals that correspond to times t_1, t_2, and t_3 will propagate into the estimated interval angular rotation rates as anti-correlated errors at the interval boundaries. The anti-correlated errors described above are the predominant cause of the classic staircase pattern that is exhibited by nearly all published interval velocity histories.

One simple method for reducing the high levels of interval rotation noise described in the previous paragraph and illustrated in Fig. A5 is to derive interval rotations from every other finite rotation rather than from successive finite rotations. Although this sacrifices some of the temporal resolution of the underlying data, the staggered intervals reduce the overall noise by increasing the time that is spanned by each interval (and hence improving the signal-to-noise ratio) and by reducing the number of anti-correlated errors between the interval rotations. A comparison of these staggered best-fitting interval velocities (gray circles in Fig. A5) to the shortest-interval velocities (red triangles) illustrates the reduction in noise for the former relative to the latter velocity estimates.

The Bayesian noise-reduction method employs a different approach, whereby smoothing of the underlying observations via time averaging or splining is abandoned in favor of an approach that identifies from ensembles of millions of possible rotation sequences the suite of models that represent the simplest realization of the original rotations based on pre-defined Bayesian criteria (Iaffaldano *et al*. 2012, 2014). Since no smoothing or averaging is employed for the analysis, the full temporal resolution of the starting rotations is preserved.

The Bayesian interval velocities shown in Fig. A5 clearly define a simpler kinematic history than do the velocities determined from the best-fitting finite rotations. In particular, the best-fitting velocities that sample the shortest intervals (red triangles) vary by a factor of 5-10 more than do the Bayesian interval velocities (red line), which have the same sampling frequency. That the spline-smoothed interval velocities (brown line), agree well with Bayesian estimates gives us confidence in the robustness of the results.

Table 1: North America-Pacific best-fitting finite rotations and rotation covariances

Chron	Age	Lat.	Long.	Ω	Covariances					
	(Myr)	(°N)	(°E)	(deg.)	a	b	c	d	e	f
1n	0.781	48.03	286.80	-0.553	1.5	-0.6	-0.4	1.0	0.8	1.5
2n	1.778	48.71	286.21	-1.281	7.0	1.9	-9.0	1.6	-1.4	19.6
2An.1	2.581	48.29	286.78	-1.821	8.7	1.1	-6.0	1.9	0.1	15.0
2An.3	3.596	48.27	288.52	-2.593	18.7	5.0	-16.5	4.3	-2.3	34.0
3n.1	4.187	48.88	288.35	-2.985	24.1	6.9	-22.9	5.4	-2.7	48.2
3n.4	5.235	50.11	287.64	-3.773	30.4	6.7	-27.4	4.8	-4.5	53.1
3An.1	6.033	50.61	286.95	-4.340	26.4	4.2	-19.6	6.1	1.8	50.8
3An.2	6.733	51.14	286.21	-4.873	32.3	2.8	-32.8	4.0	-2.9	66.0
4n.1	7.528	51.35	287.29	-5.360	42.3	5.4	-42.7	5.8	-6.8	76.7
4n.2	8.108	51.70	287.53	-5.779	42.6	2.9	-43.0	8.9	-6.2	94.2
4A	9.105	51.46	289.02	-6.278	70.5	1.2	-70.3	12.7	-13.4	108.2
5n.1	9.786	51.42	291.17	-7.033	97.3	19.1	-96.2	13.6	-25.1	141.6
5n.2	11.056	52.86	290.12	-7.729	29.2	2.9	-27.3	7.4	-0.9	60.5
5An.2	12.474	53.48	291.50	-8.671	28.8	1.7	-36.3	5.9	-5.2	68.6
5AC	13.739	53.74	292.72	-9.503	26.9	0.6	-22.6	5.5	-1.7	43.5
5AD	14.609	53.62	293.18	-10.061	38.0	0.7	-35.6	6.8	-1.3	59.2
5Cn.1	15.974	54.10	293.49	-10.688	206.6	-6.0	-249.7	31.8	-23.2	413.6
5D	17.235	54.46	293.47	-11.392	206.5	-12.1	-251.1	30.2	-20.0	410.6
5E	18.056	54.60	293.50	-11.799	203.6	-11.4	-251.6	31.5	-16.6	411.6
6ny	18.748	54.38	293.33	-12.219	431.2	-95.8	-326.1	56.7	68.5	323.6
6no	19.722	56.65	289.71	-12.864	90.5	14.8	-50.6	38.3	2.9	92.6

These rotations reconstruct the North America plate onto the Pacific plate. The rotation angles Ω are positive anticlockwise. The rotations and their covariances are determined from the North America-Nubia, Nubia-Antarctic, and Antarctic-Pacific best-fitting rotations using methods described in the text. The covariances, which have units of 10^{-8} radians^2, are tied to the Pacific plate.

Table 2: Sierra Nevada-Great Valley microplate relative to Pacific plate finite rotations.

Chron	Age	Lat.	Long.	Ω	Covariances					
	(Myr)	(°N)	(°E)	(degrees)	a	b	c	d	e	f
Uses *d'Alessio et al. 2005* SNGV-NA motion estimate										
1n	0.781	45.72	276.10	-0.533	4.7	2.9	-4.5	6.9	-4.6	6.9
2n	1.778	45.93	275.79	-1.215	12.9	15.2	-16.0	30.8	-24.3	25.7
2An.1	2.581	46.10	275.64	-1.761	24.1	32.1	-31.5	63.6	-51.5	51.3
2An.3	3.596	46.44	275.53	-2.452	44.4	61.8	-59.3	123.3	-100.2	97.6
3n.1	4.187	46.71	275.45	-2.856	59.5	83.0	-79.7	168.1	-136.1	132.5
3n.4	5.235	47.27	275.12	-3.570	92.1	126.5	-123.1	268.0	-214.8	206.2
3An.1	6.033	47.75	274.80	-4.109	123.8	162.9	-162.2	364.3	-288.1	271.2
3An.2	6.733	48.09	274.63	-4.577	157.1	196.0	-199.8	465.2	-361.6	336.6
4n.1	7.528	48.32	274.62	-5.096	199.7	234.9	-244.6	597.8	-456.5	419.1
4n.2	8.108	48.50	274.77	-5.467	233.6	268.6	-280.1	697.1	-531.2	485.0
4A	9.105	48.94	275.36	-6.097	292.3	347.7	-350.8	851.7	-665.5	609.8
5n.1	9.786	49.30	275.81	-6.528	335.2	412.9	-405.0	957.5	-763.8	703.9
5n.2	11.056	50.03	276.55	-7.323	419.7	550.5	-519.9	1173.0	-965.4	898.3
Uses *McCaffrey 2015* SNGV-NA motion estimate										
1n	0.781	43.94	268.08	-0.650	4.7	2.9	-4.5	6.9	-4.6	6.9
2n	1.778	44.13	267.80	-1.480	12.9	15.2	-16.0	30.8	-24.3	25.6
2An.1	2.581	44.30	267.63	-2.146	24.2	32.1	-31.6	63.6	-51.5	51.2
2An.3	3.596	44.61	267.47	-2.989	44.4	61.8	-59.3	123.2	-100.2	97.6
3n.1	4.187	44.85	267.35	-3.481	59.6	83.0	-79.7	168.0	-136.2	132.5
3n.4	5.235	45.33	267.00	-4.351	92.3	126.4	-123.1	267.8	-215.0	206.2
3An.1	6.033	45.73	266.65	-5.010	124.2	162.7	-162.0	363.9	-288.5	271.3
3An.2	6.733	46.03	266.44	-5.583	157.7	195.8	-199.5	464.3	-362.4	336.9
4n.1	7.528	46.23	266.35	-6.219	200.6	234.6	-243.9	596.2	-457.8	419.7
4n.2	8.108	46.40	266.41	-6.675	234.7	268.2	-279.1	695.0	-532.9	485.9
4A	9.105	46.83	266.73	-7.448	293.6	347.4	-349.6	849.1	-667.5	611.1
5n.1	9.786	47.17	266.97	-7.976	336.4	412.8	-403.7	954.8	-765.7	705.5
5n.2	11.056	47.85	267.34	-8.949	420.8	550.7	-518.8	1170.1	-967.0	900.1

The above rotations, which reconstruct the Sierra Nevada-Great Valley microplate onto the Pacific plate, were determined by combining the Pacific-North America rotations from Table 5 in the main document with the rotation of the Sierra Nevada-Great Valley microplate relative to North America as extrapolated back in time from the geodetic estimates of d'Alessio *et al.* (2015) (9.54 °N, 137.41 °W, -0.231 ° Myr^{-1}) and McCaffrey (2015) (26.1 °S, 196.7 °E, -0.113 ° Myr^{-1}. Rotation angles Ω are positive CCW. The covariances are calculated in a Pacific plate reference frame and have units of 10^{-8} $radians^2$.

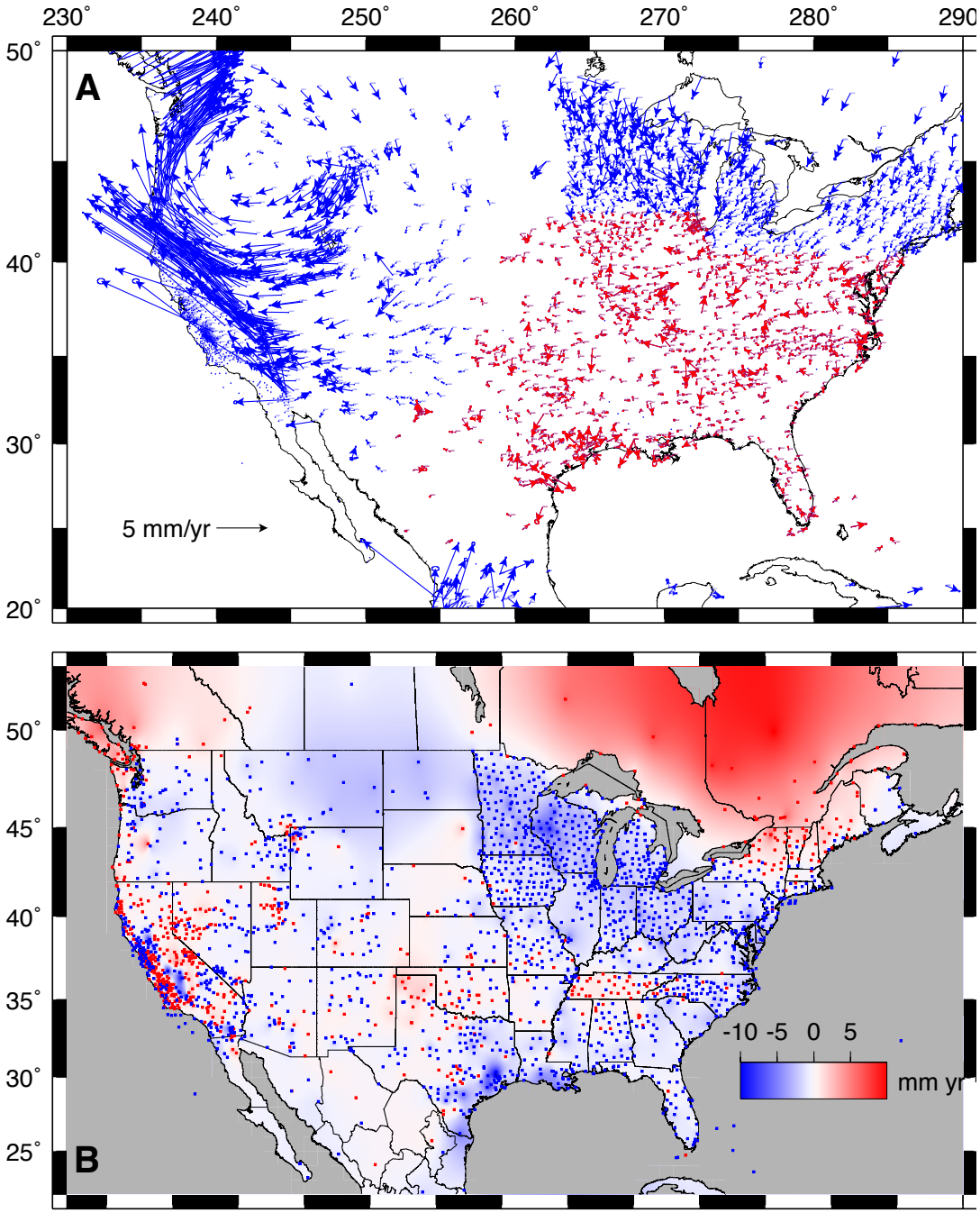

Fig. A1. A - Motions of North America plate continuous GPS sites corrected for the rotation of the North America plate in IGS08. The angular velocity that was used to correct all of the GPS site velocities shown in Panel A is given in Table 1 of the main paper and was derived from the velocities of 908 intraplate stations, as described and illustrated in the main paper. The velocities shown in red and blue show GPS sites whose velocities that were and were not used to estimate the best-fitting North America-IGS08 angular velocity, For clarity, sites moving faster than 12 mm yr^{-1} were omitted from the figure. respectively. B - Distribution of vertical rates in IGS08. Auxiliary Figure 2 shows additional detail for the vertical rates. Site names in Panel A are visible on high magnification.

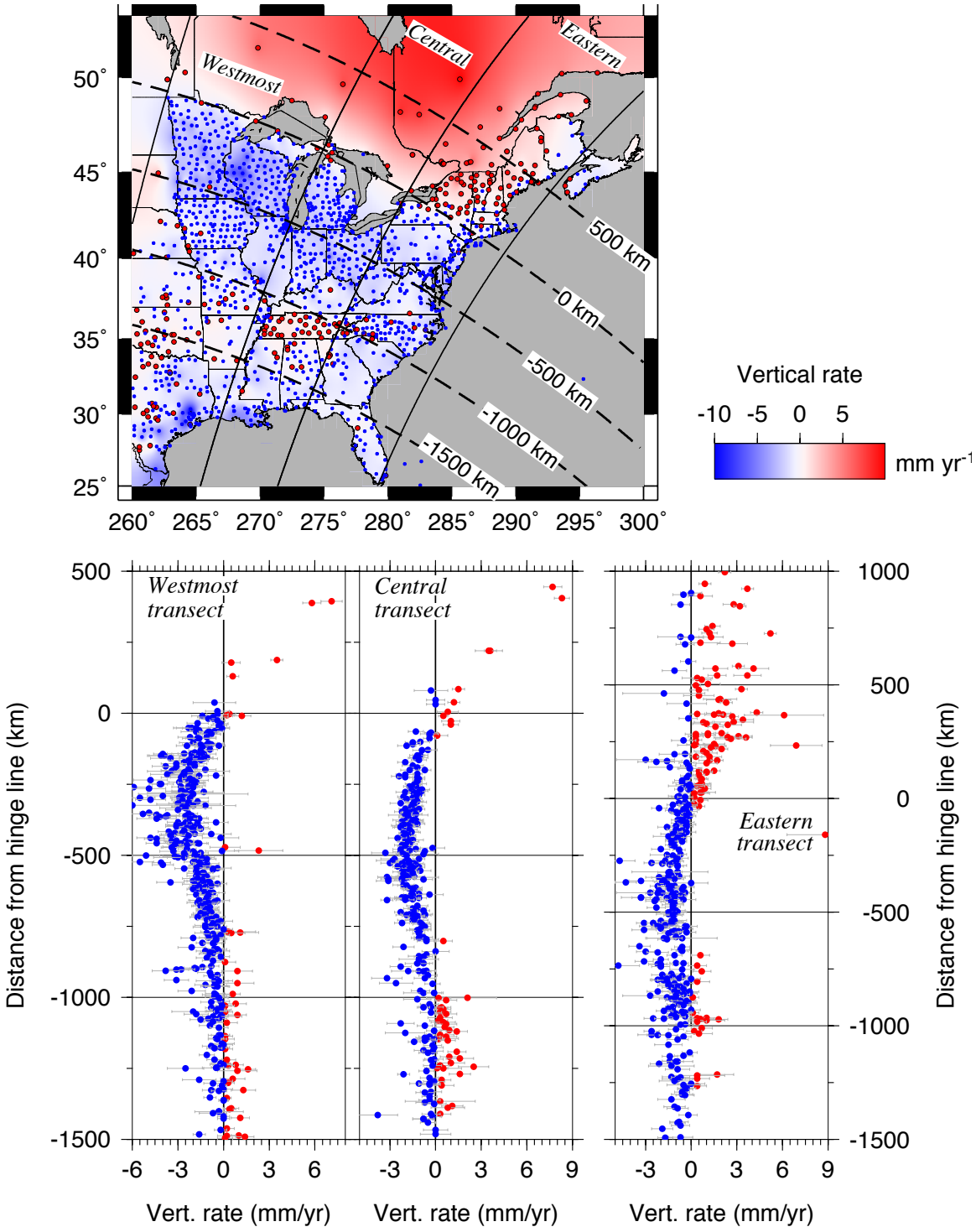

Fig. A2. Vertical rates in areas of the North America plate interior with high concentrations of GPS sites and glacial isostatic rebound. The upper map subdivides the eastern half of North America into three NNE-oriented transects that are roughly orthogonal to the hinge line (at 0 km) that separates areas of glacial isostatic uplift from areas that are subsiding. The three transects below the map show vertical GPS site rates as a function of great-circle distance orthogonal to the hinge line.

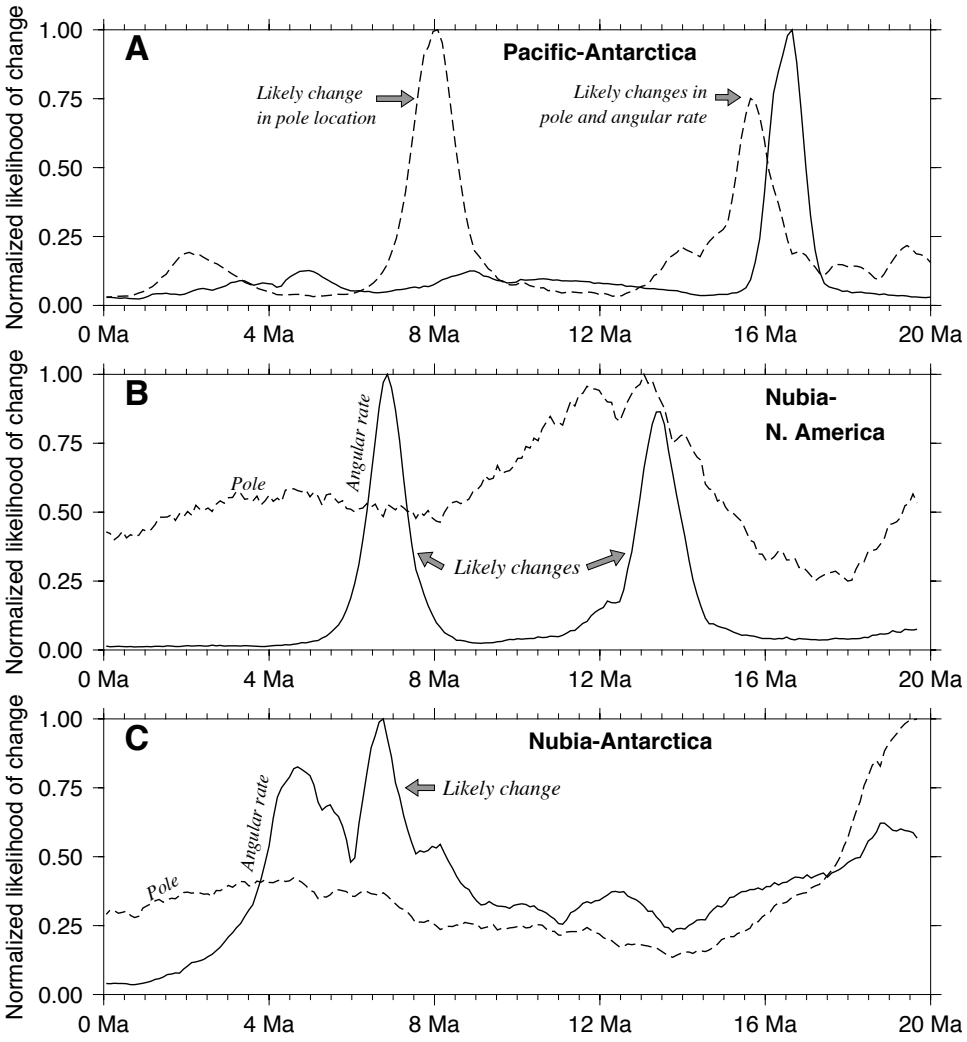

Figure S3. Likelihood of changes in pole locations (dashed lines) and angular opening rates (solid lines) during the past 20 Myr for the Pacific-Antarctic (A), Nubia-North America (B), and Nubia-Antarctic (C) plate pairs from REDBACK (Bayesian) analyses of their respective best-fitting rotation sequences (see text). Narrow peaks define periods when well-timed changes in motion were the most likely to have occurred. The likelihood of change within the millions of models that were sampled for the Bayesian analysis is normalized to 1.0.

Fig. A3. Likelihood of changes in pole locations (dashed lines) and angular opening rates (solid lines) during the past 20 Myr for the Pacific-Antarctic (A), Nubia-North America (B), and Nubia-Antarctic (C) plate pairs from REDBACK (Bayesian) analyses of their respective best-fitting rotation sequences (see text). Narrow peaks define periods when well-timed changes in motion were the most likely to have occurred. The likelihood of change within the millions of models that were sampled for the Bayesian analysis is normalized to 1.0.

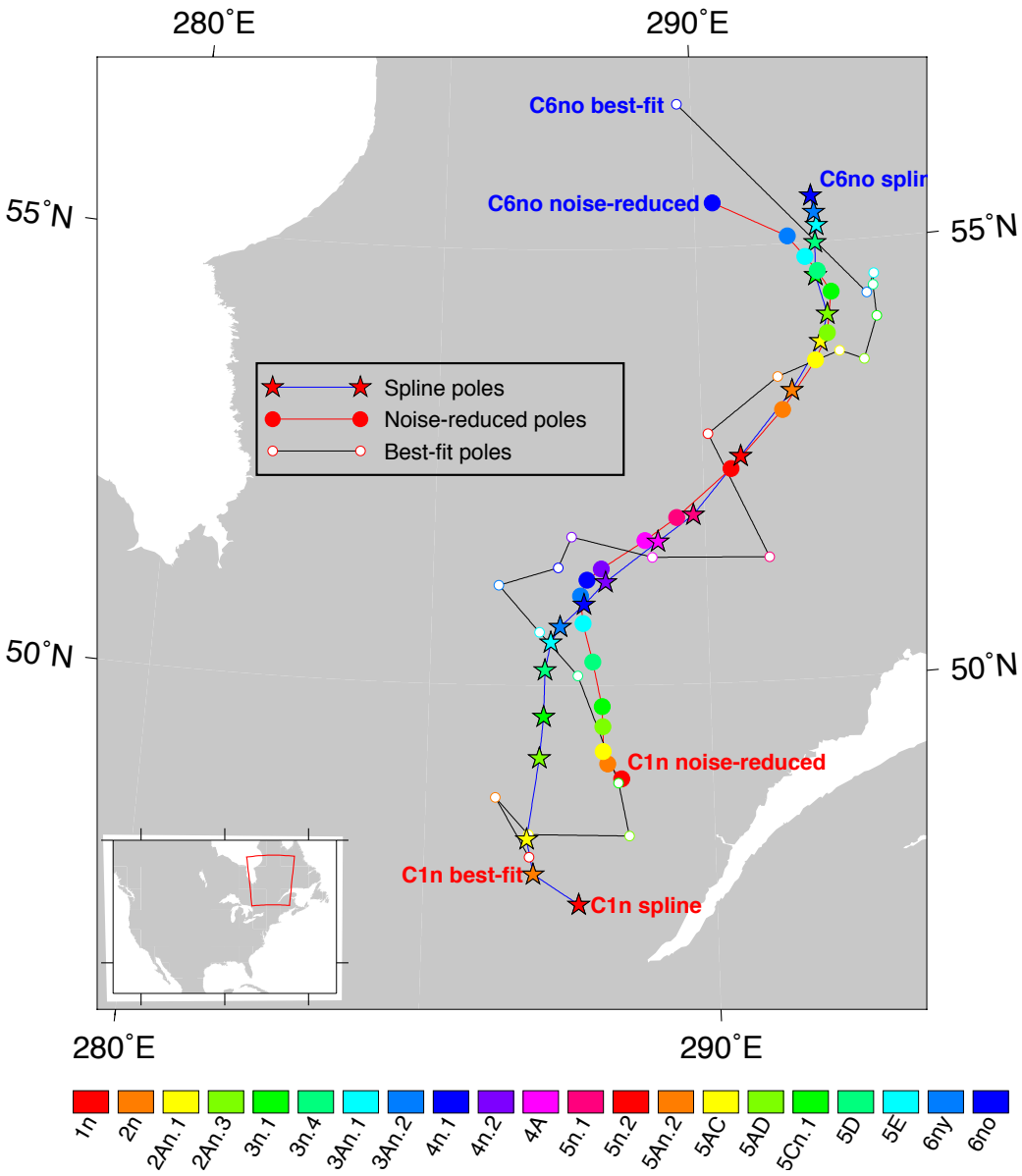

Fig. A4. Pacific-North America best-fitting, noise-reduced, and spline poles. The latter poles were derived using the cross-validation method of Hanna & Chang (2000), as discussed in the text. As shown in the legend, solid circles connected by the red line show the noise-reduced, finite rotation poles, open circles connected by the black line show the best-fitting finite rotation poles, and stars connected by the blue line show the spline poles.

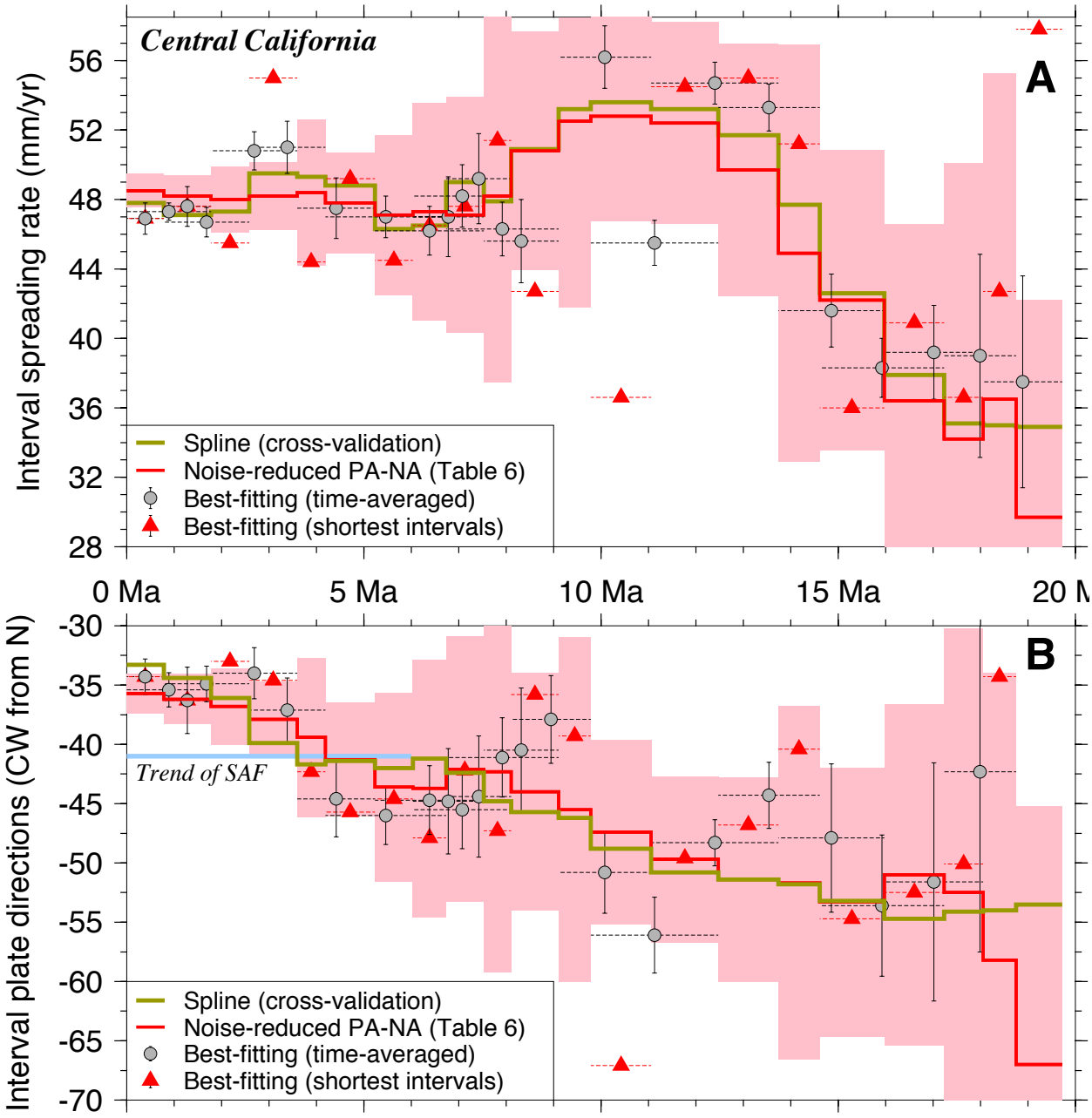

Fig. A5. Comparison of Pacific plate interval rates (A) and directions (B) relative to the North America plate estimated with stage angular velocities determined from the best-fitting, noise-reduced, and spline-smoothed finite rotations. Velocities are estimated at 36.0 °N, 120.6 °W along the San Andreas fault of central California. Two sets of interval velocities were derived from the best-fitting finite rotations in Table 4. One, shown by the red triangles, averages motion over the shortest possible intervals between the finite rotations. The other, shown by the gray circles, employs longer averaging intervals (0.8-2 Myr) as a means of suppressing noise. The horizontal dashed lines show the averaging interval that each velocity spans. All uncertainties are one-sigma and are propagated from the interval rotation covariances. The light blue line in (B) shows the San Andreas Fault (SAF) azimuth in central California.

References in addition to those provided in the main document

Bennett, R. A., Davis, J. L., & Wernicke, B. P., 1999. Present-day pattern of Cordilleran deformation in the western United States, *Geology*, **27**,,371–374.

Bertiger, W., Desai, S. D., Haines, B., Harvey, N., Moore, A. W., Owen, S., & Weiss, J. P., 2010. Single receiver phase ambiguity resolution with GPS data, *J. Geodesy*, **94**,,327–337.

Calais, E., Han, J. Y., DeMets, C., & Nocquet, J. M., 2006. Deformation of the North American plate interior from a decade of continuous GPS measurements, *J. Geophys. Res.* **111, B06402**, doi: 10.1029/2005JB004253.

Kreemer, C., Blewitt, G., & Bennett, R. A., 2010. Present-day motion and deformation of the Colorado Plateau, *Geophys. Res. Lett.*, **37 37, L10311**, doi: 10.1029/2010GL043374.

Marquez-Azua, B., & DeMets, C., 2009. Deformation of Mexico from continuous GPS from 1993 to 2008, *Geochem. Geophys. Geosyst.*, **10, Q02003**,,doi:10.1029/2008GC002278.

Sella, G. F., Stein, S., Dixon, T. H., Craymer, M., James, S., Mazzotti, S., & Dokka, R. K., 2007. Observation of glacial isostatic adjustment in "stable" North America with GPS, *Geophys. Res. Lett.*, **34 (L02306)**,,doi:10.10292006GL027081.